

# EFFECT OF ELEMENTAL SEGREGATION ON THE MICROSTRUCTURE AND MECHANICAL PROPERTIES OF HEAVY SECTION COMPACTED GRAPHITE IRON

Qizhou Cai , Zhe Chen and Can Xu

State Key Laboratory of Materials Processing and Die and Mould Technology, School of Materials Science and Engineering, Huazhong University of Science and Technology, Wuhan 430074, People's Republic of China

Pinjun Wan, Bokui Hao and Xiaozhou Deng

Yichang Marine Diesel Engine Co. Ltd., Yichang 443002, Hubei, People's Republic of China

Copyright © 2022 American Foundry Society  
<https://doi.org/10.1007/s40962-022-00758-0>

## Abstract

*The effect of elemental segregation on the microstructure and properties of heavy section compacted graphite iron (CGI) was studied to develop a type of CGI cylinder liner for marine low-speed diesel engine. It is found that the nodularity in heavy section of the cylinder liner showed obvious difference due to the different cooling rates and segregation of cerium (Ce) and magnesium (Mg). The exterior and interior samples of the heavy section with higher cooling rate and lower Ce and Mg segregation had the lower nodularity of 8% and 13%, respectively. While the nodularity of central samples was up to 20% and the nodule size was also larger than those of exterior and interior samples. Ce and Mg segregated into the post solidified molten iron, resulting in the formation of bulk or nodular graphite. The CGI matrix was composed of pearlite and a small amount of eutectic carbide. Segregation of carbide forming elements promoted the formation of*

*carbides at eutectic boundaries. The carbide content of central sample was 3%, higher than those of exterior sample (2.1%), and interior sample (2.5%). The tensile strength, elongation, and hardness of central samples were 383 MPa, 0.42%, and 248 HBW, respectively, which were lower than exterior sample of 400 MPa, 0.52%, and 252 HBW, and interior sample of 388 MPa, 0.43%, and 250 HBW. The fracture morphologies of tensile samples were characterized by cleavage facets and a few torn edges, showing the typical brittle fracture. The carbides and shrinkage porosities promoted the initiation and propagation of cracks.*

**Keywords:** cylinder liner, compacted graphite iron, elemental segregation, microstructure, mechanical properties

## Introduction

Compacted graphite iron (CGI) has higher tensile strength, thermal fatigue resistance, and dimensional stability than gray iron and better thermal conductivity and damping properties than nodular iron, which could meet the requirements of cylinder liner for the modern marine low-speed diesel engine on material mechanical properties, thermal conductivity, and antifricition performance.<sup>1-4</sup> The strength, stiffness, antifricition and thermal fatigue properties of cylinder liner prepared by using CGI could be improved significantly.<sup>5-7</sup> Compared with the alloyed gray

cast iron cylinder liner, CGI can reduce the amount of alloying elements and the production cost, and improve the profit and competition of products.

The new generation of marine low-speed diesel engine is developing toward high intensity, super long stroke, super high burst pressure and effective pressure, and high output power.<sup>8-10</sup> These engines are of large size, with length, width, and height reaching tens of meters. The cylinder liner for the marine low-speed diesel engine is often large in diameter. Its height is greater than 2000 mm and section thickness is more than 100 mm, which belongs to heavy section CGI casting. Usually, CGI alloyed with Cr, Mo, Ni, Cu, and B is used to obtain the matrix of pearlite and a certain amount of hard phase to improve the strength,

hardness, and wear resistance of cylinder liner.<sup>11–13</sup> However, the long solidification time due to the large heat capacity and slow cooling rate of the heavy section cylinder liner castings promotes graphite coarsening and graphite degradation. While the elemental segregation also provides the condition for graphite degradation, and the probability of graphite floating increases significantly.<sup>14,15</sup> On the other hand, Cr, Mo, and other strong carbide forming elements are positive segregation elements, which are inclined to segregate at the eutectic boundaries, increase the chilling tendency of molten iron, promote the formation of carbides, deteriorate the microstructure and the properties of CGI cylinder liner.<sup>16,17</sup>

The main aim of the present study was to analyze the effect of elemental segregation on the microstructure and properties of heavy section CGI by means of microstructure observation, elemental segregation analysis, and mechanical properties test. The fracture mechanism was discussed by fracture analysis. The results will provide experimental basis for microstructure and properties control of heavy section CGI.

## Experimental Procedure

### Casting Procedure

High purity pig iron, scrap steel, and master alloys such as ferrochromium, ferrovanadium, ferromolybdenum, metallic Cu, etc., were selected as charging materials. Molten iron was melted in a capacity of 20 t medium frequency induction furnace, adjusting the carbon content of molten iron with carburizing agent. Metallic Sn was added to the ladle according to design composition. The molten iron was heated to 1520 °C and then held for 10 min. Both 0.30–0.32 wt% REMgSiFe and 0.08–0.10 wt% RESiFe master alloys were used as vermiculizer for vermiculizing treatment by using sandwich process. 0.40–0.50 wt% BaSiFe master alloy was selected as primary inoculant in ladle, and 0.10–0.12 wt% SrSiFe master alloy with size of 0.2–0.7 mm was selected as downsprue inoculant (as shown in Figure 1). The chemical composition of vermiculizer and inoculant is shown in Table 1. Low silicon content was selected to prevent ferrite formation in the matrix of heavy section CGI castings.

Figure 1 shows the schematic diagram of CGI cylinder liner and its casting process. The height of casting is 2350 mm, and the maximum section thickness is 110 mm. The casting process was vertical molding process and top pouring. The self-hardening furan resin sand mold was used in cylinder liner casting. The sand core was a furan sand core with mandreled hollow, and its wall thickness was 50 mm (small end)–80 mm (big end). In order to prevent flake graphite casting skin formation,<sup>18–20</sup> the sand mold and core were made of all new sand, sulfonic acid

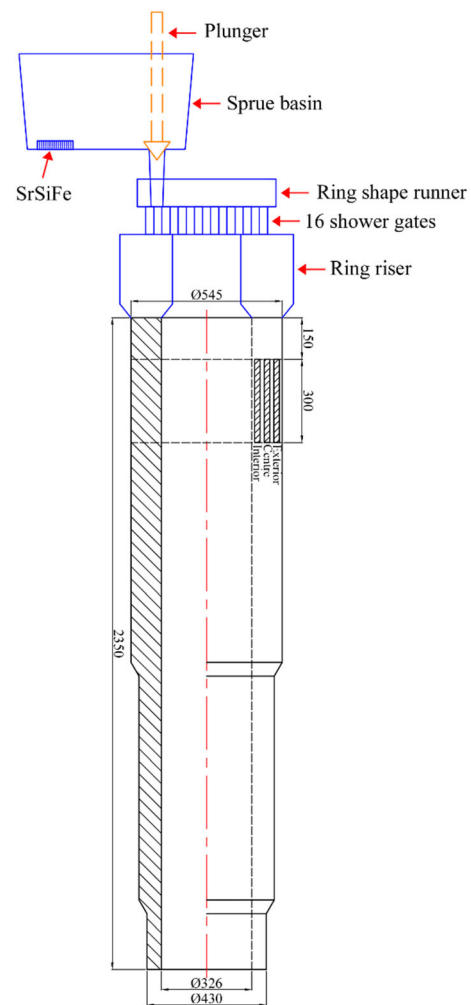


**Figure 1. Schematic diagram of CGI cylinder liner and its casting process, and sampling positions (dimensions in millimeters).**

**Table 1. Chemical Composition of Vermiculizer and Inoculant (wt%)**

Master alloys	Si	Mg	RE	Ca	Al	Ba	Sr	Fe
REMgSiFe	45	5.5	6.0	2.1	0.5			Bal.
RESiFe	45		30	1.8	1.5			Bal.
BaSiFe	72.5			1.4	1.2	3.4		Bal.
SrSiFe	75.5			0.1	0.5		0.8	Bal.

curing agent with content of 0.0–1.5% free sulfuric acid and alkaline coating. The chemical composition of the castings is listed in Table 2.

The samples were cut from the cylinder liner according to the sampling position shown in Figure 1. Firstly, a ring block with a height of 300 mm was cut from the heavy section, and then, the square samples of 20 mm × 20 mm × 300 mm were taken from the outside

**Table 2. The Chemical Composition of the Cylinder Liner Castings (wt%)**

C	Si	Mn	P	S	Ni	Cr	Mo
3.90–4.00	1.50–1.60	0.70–0.80	< 0.025	< 0.012	0.20–0.30	0.15–0.25	0.20–0.30
Cu	Sn	Ce + La	Mg	Ba, Sr	Fe		
1.60–1.80	0.04–0.06	0.020–0.023	0.008–0.010	trace	bal.		

Carbon equivalent,  $CE = C + 1/3Si = 4.40\text{--}4.53\%$

to the inside. The exterior sample was 10 mm away from the outer surface of the casting, while the interior sample was taken 10 mm away from the inner surface of the casting. The square samples were processed into tensile samples as shown in Figure 2. After the tensile testing, the metallographic observation sample ( $\varphi 20\text{ mm} \times 10\text{ mm}$ ) and hardness measurement sample ( $\varphi 20\text{ mm} \times 15\text{ mm}$ ) were machined from the tensile sample head. Three castings of trial cylinder liners were selected to examine the microstructure and properties. Nine samples were cut from each casting, including three samples for the exterior, center, and interior, respectively.

### Microstructure Characterization

After the metallographic sample was ground and polished, the graphite morphology was observed by using the Caikon DMM-480C metallographic microscope. Graphite from ten visual fields of each sample was selected to evaluate the nodularity according to ISO16112. The matrix of the sample by chemical etching Nital 4% was observed, and ten visual fields of each sample were selected for statistical analysis of the number of carbides. The microstructure of the sample was observed by FEI Quanta 200 field emission scanning electron microscope (FSEM), and the element segregation was analyzed by energy dispersive spectroscopy (EDS).

### Mechanical Properties Testing

The tensile test was carried out on the Shimadzu AG-IC/100 kN materials testing machine with the loading speed of 1 mm/min, and the tensile strength and elongation of the

CGI were measured. The fracture morphologies of the sample were observed by using FSEM. The hardness of the sample was measured by Wilson BH3000/T Brinell hardness tester, with a load of 3000 kg and a holding time of 15 s.

## Results and Discussion

### Microstructure

#### Graphite Morphologies

Figure 3 shows the graphite morphologies of cylinder liner casting. It can be seen from Figure 3a that the graphite in exterior sample was fine and evenly distributed with low nodularity of  $(8 \pm 3)\%$ . Figure 3c shows the graphite morphology of the interior sample with nodularity of  $(13 \pm 5)\%$ . Based on the calculation results of solidification simulation CAE software, the cooling rate of the interior sample was slower than that of the exterior sample, because the sand core was cooled under the surrounding of molten iron. Therefore, the graphite size was larger than that of the exterior sample, and a small amount of nodule or bulk graphite was formed at the eutectic boundaries. The uniformly distributed compacted graphite could not only significantly reduce the notch effect on the matrix, but also make full use of the lubrication effect of graphite, thereby improving the antifriction property of cast iron.<sup>21,22</sup> However, it can be seen from Figure 3b that the graphite morphologies, size, and distribution uniformity of the central sample were inferior to those of the exterior sample and interior sample, and the nodularity was up to  $(20 \pm 5)\%$ . The nodule size was also higher than those of exterior and interior samples. From the compacted graphite clusters

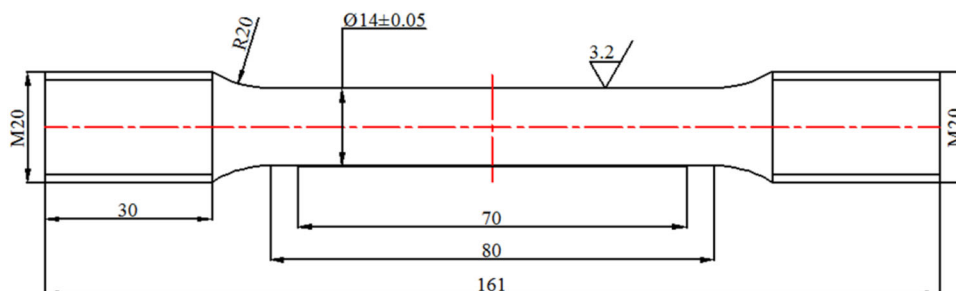


**Figure 2. Shape and size of tensile sample (dimensions in millimeters).**

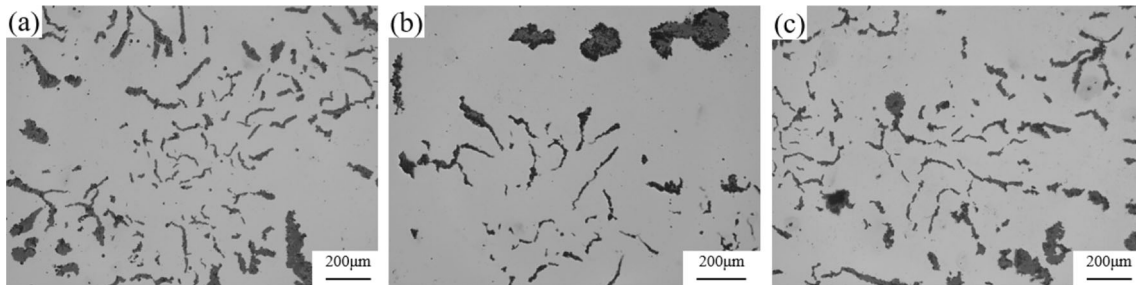


**Figure 3. Graphite morphologies (magnification 50×) of cylinder liner heavy section: (a) exterior sample, (b) central sample, (c) interior sample.**

and distribution of nodular graphite shown in Figure 3, it can be seen that the central sample had large size eutectic cells and wide eutectic boundaries. Because the heat released in the center (including sensible heat and latent heat) needed to be lost through the solidified layer of the outer and inner layers, at this moment, the cooling capacity of the sand mold and sand core decreased greatly, and the cooling rate in the center was the lowest. The longer solidification time in the center led to the increase of graphite size and the formation of bulk and spherical graphite. It can be seen that the graphite morphologies of heavy section have obvious difference due to the different cooling rates.

#### *Pearlite and Carbide*

The matrix microstructure of cylinder liner heavy section was shown in Figure 4. The metallographic microstructure shows that the matrix of the cylinder liner heavy section was composed of pearlite and a small amount of carbides, and there was no obvious difference in the pearlite of the exterior, central, and interior samples. For the antifriction cast iron, increasing the hardness of the matrix can reduce wear. But, the matrix with too high hardness is not conducive to graphite film formation (the graphite in cast iron is extruded by friction to form the graphite film between the friction pairs during the sliding friction process). Considering the effects of hardness and graphite film formation, the matrix of pearlite is the most suitable for the antifriction cast iron. The more pearlite, the narrower the

spacing, the better the friction and wear properties of cast iron.<sup>23,24</sup>

It can also be seen from Figure 4 that there were obvious differences in the amount of carbides in the exterior, central, and interior samples of cylinder liner casting. The statistical results of carbides content were as follows:  $(2.1 \pm 0.2) \%$  for exterior samples,  $(3 \pm 0.3) \%$  for central samples,  $(2.5 \pm 0.2) \%$  for interior samples, the carbide content in the central samples was the highest. This is due to the low silicon content, and the carbide forming elements segregation, which increased the chilling tendency and promoted the formation of carbides at the eutectic boundaries. The appropriate amount of carbides can play the role of support in the matrix, which is beneficial to maintaining lubricant and reducing friction and wear of cast iron. But the excessive carbides reduce the mechanical properties of castings, especially the plasticity and toughness, and become the crack source in the process of friction and wear. Moreover, if the carbide falls off from the matrix, it becomes abrasive and accelerates the wear of cylinder liner. Therefore, for large marine cylinder liner, the amount of carbides should be controlled in a reasonable range to ensure good comprehensive performance.

The morphology and composition of carbide were analyzed. Its morphology is shown in Figure 5, and the chemical composition of carbide is listed in Table 3. As shown in Figure 5, a few pearlites were distributed in the carbide, which was the transformed ledeburite. The pearlite was small in number and fine in structure, and its lamellae were not easy to observe. Secondary cementite was

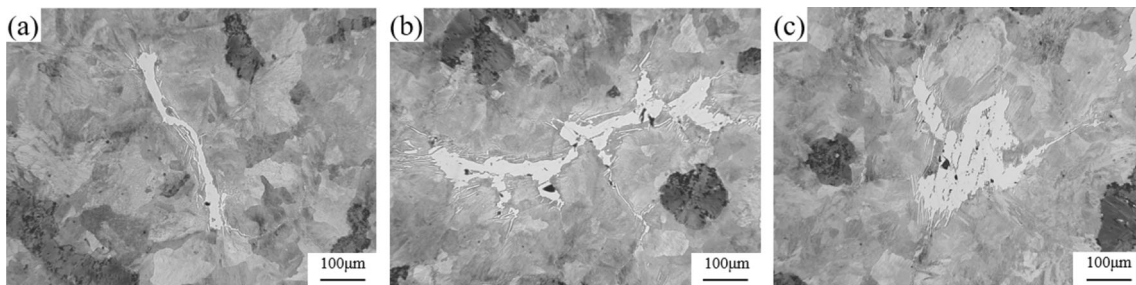


**Figure 4. Matrices (magnification 100×) of cylinder liner heavy section: (a) exterior sample, (b) central sample, (c) interior sample.**

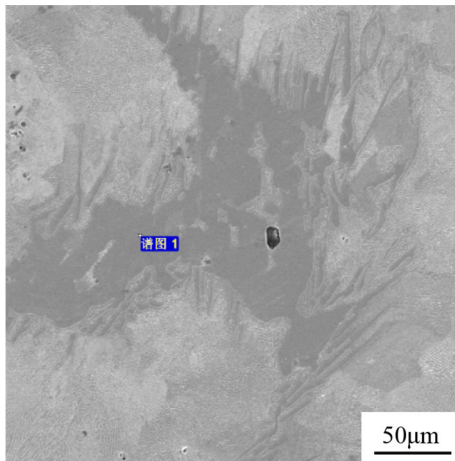


**Figure 5. Carbides in matrix.**

**Table 3. The Composition of Carbide in Figure 5**

Elements	wt%	at%
C	10.53	35.92
Cr	2.40	1.89
Mn	2.67	1.99
Mo	5.60	2.39
V	0.28	0.22
Fe	78.53	57.59

distributed around the primary carbide, and the secondary cementite precipitates along a certain habit plane of austenite in acicular to form Widmanstatten structure.

It can be seen from the chemical composition in Table 3 that the content of alloying elements of Cr, Mn, Mo, and V in the carbide was higher than that in Table 2. This was because the carbide forming elemental segregation increased the chilling tendency of molten iron, eutectic carbides formed at the eutectic boundaries based on the

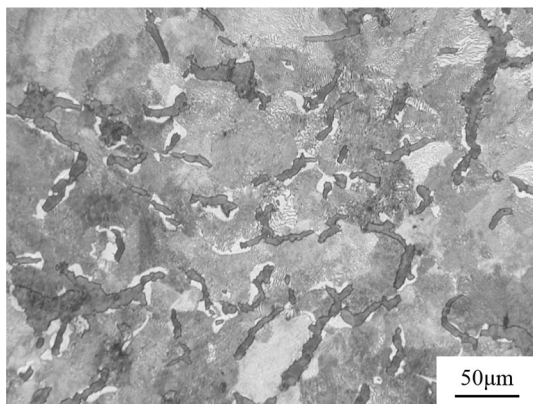


**Figure 6. Ferrite in the matrix of the exterior sample (magnification 200×).**

metastable Fe–Fe<sub>3</sub>C phase diagram. It can also be seen from the data in Table 3 that the content of Mo in the composition of casting was 0.20–0.30 wt%, while the content of Mo in the carbide was as high as 5.6 wt%, indicating that the segregation of Mo in casting was serious. On the other hand, from the morphology of carbides, Mo segregation did not form Mo carbides, but solid solution in cementite to form alloying cementite.

Figure 6 shows the ferrite in the matrix of the exterior sample. The result shows that a small amount of ferrite precipitated in the dense area of fine graphite. The precipitation of ferrite would reduce the strength and wear resistance of cast iron. Generally, the matrix of as-cast CGI has a strong tendency of ferrite formation, because the dense branching of graphite shortens the path of carbon diffusion.<sup>25</sup> The low silicon content and pearlite promoting elements Cu, Cr, Mn, etc., promote the formation of pearlite and inhibit the formation of ferrite, which can meet the requirements of cylinder liner for ferrite amount control.

Based on the above microstructure analyses, the microstructure characteristic parameters of the heavy section are listed in Table 4.

### Effect of Elemental Segregation on Microstructure

#### Segregation of Spheroidizing Elements

The graphite morphology at eutectic boundary and the distribution of spheroidizing elements are shown in Figure 7. As can be seen from Figure 7a, a certain amount of bulk and spherical graphite formed at the boundaries of eutectic cells, the distribution of carbon and spheroidizing elements Ce and Mg at the eutectic boundaries was analyzed by EDS. The results are shown in Figure 7b–d. From the distribution of elements Ce and Mg, it can be seen that the spheroidizing elements Ce and Mg increased toward spherical graphite. This is because Ce and Mg are positive segregation elements in molten iron, while the cooling speed in the center of thick section was slow. With the progress of solidification process, Ce and Mg were segregated in the molten iron at the boundaries of eutectic cells. The amount of Ce and Mg in molten iron increased, and the graphite morphology changed from compacted graphite to near nodular graphite. The graphite grew rapidly and had a large size due to long solidification time.

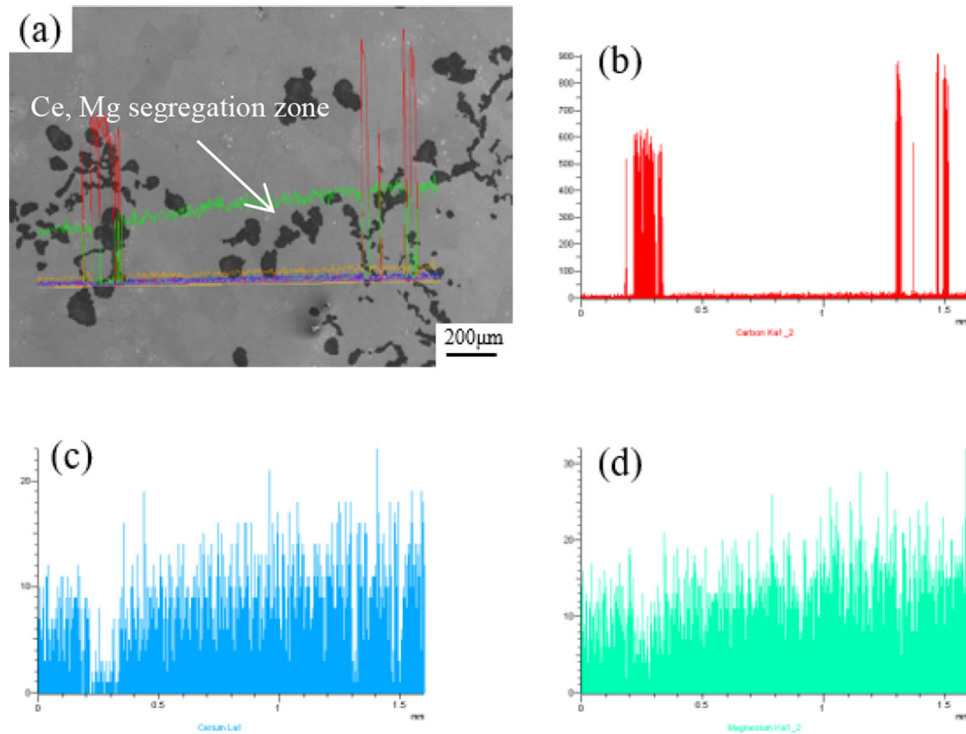
#### Segregation of Carbide Forming Elements

Figure 8 shows the carbides at the eutectic boundary and the EDS line scanning spectra for alloying elements across carbide. It can be seen from Figure 8a that the carbides

**Table 4. The Nodularity, Nodule Size, Ferrite/Pearlite, and Carbide Content of the Heavy Section**

Samples	Nodularity/%	Nodule size/ $\mu\text{m}$	Pearlite*/%	Ferrite/%	Carbides/%
Exterior	$8 \pm 3$	$60 \pm 20$	$96.9 \pm 0.2$	1	$2.1 \pm 0.2$
Centre	$20 \pm 5$	$85 \pm 35$	$97.0 \pm 0.3$	0	$3.0 \pm 0.3$
Interior	$13 \pm 5$	$75 \pm 25$	$97.5 \pm 0.2$	0	$2.5 \pm 0.2$

\*Pearlite + ferrite + carbide = 100%



**Figure 7. Graphite morphology and distribution of elements C, Ce and Mg at eutectic boundary: (a) graphite morphology, (b) element C, (c) element Ce, (d) element Mg.**

were network morphology. The element distributions in Figure 8b–g show that the contents of Mn, Cr, and Mo in carbides were high, while the contents of Si and Cu were low. Moreover, it can be seen from the results in Figure 7 that the spheroidizing elements Ce and Mg were also segregated at the eutectic boundaries. Under the synthetic action of spheroidizing elements and carbide forming elements, the chilling tendency of molten iron at the eutectic boundaries was promoted to form carbides.

It can be seen from Table 4 that the central samples with the slowest cooling rate had the highest nodularity, the largest size of nodular graphite, and the highest carbide content, followed by the interior samples with the slower cooling rate. Based on the results of Figure 7 and Figure 8, such microstructural characteristics were the synergistic effect of cooling rate and element segregation.

- Ce and Mg are positive segregation elements. When the cooling rate was slow, Ce and Mg were segregated in molten iron at the eutectic boundaries during solidification. Although there was a certain depletion of Mg in solidifying molten iron, the content of Ce in vermiculizer was much higher than that of Mg, and the Ce residual content was higher. The segregation of Ce promoted the graphite nodularization and improved the nodularity. This segregation of Ce and Mg has been confirmed in the inverse chill of ductile iron.<sup>26</sup>
- Cr, Mo, and other carbide forming elements are also positive segregation elements. With the progress of solidification, these alloying elements were segregated in the molten iron at the eutectic boundaries, while the content of negative segregation element Si was low, therefore, the eutectic undercooling at the eutectic boundaries increased. According to the relationship between eutectic

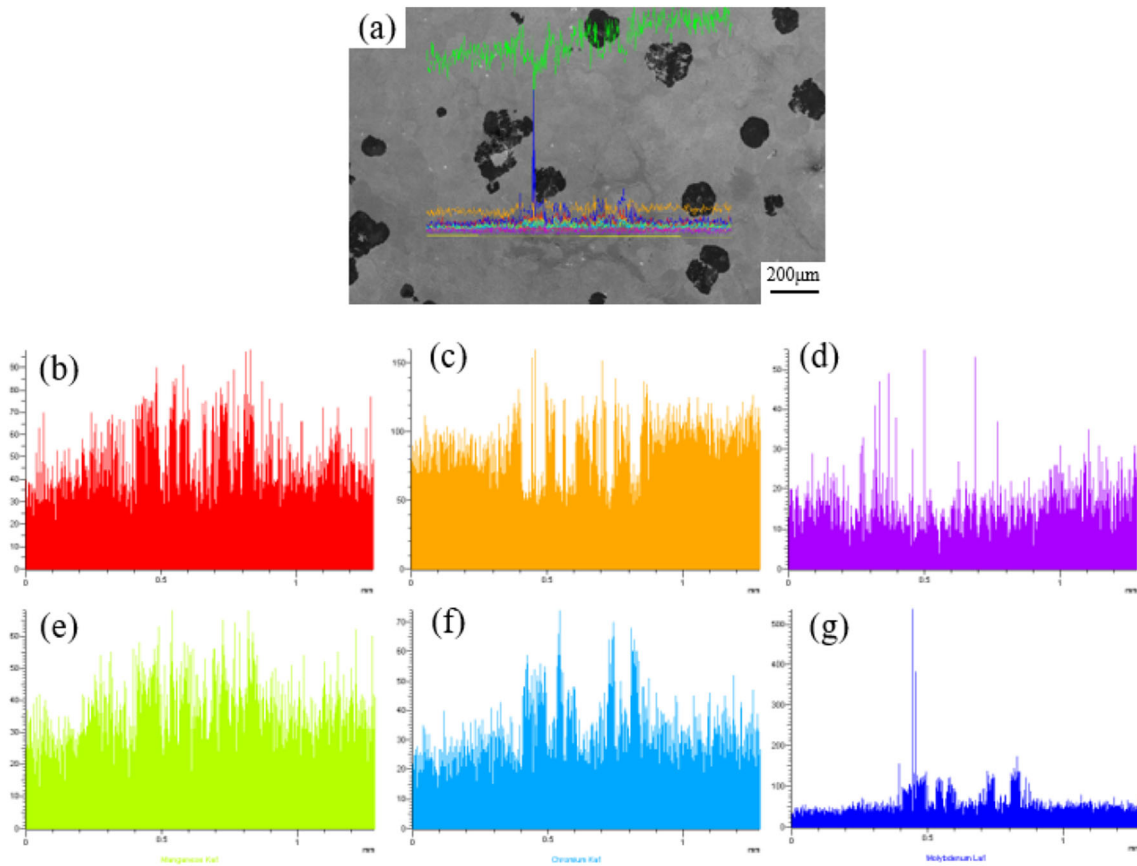


**Figure 8. Network carbides and alloying elements distribution: (a) net carbide, (b) C, (c) Si, (d) Cu, (e) Mn, (f) Cr, (g) Mo.**

temperature and nodularity,<sup>27</sup> when the eutectic temperature decreases, the graphite tends to be spheroidized, the nodularity increases, showing similar effect of the cooling rate on the nodularity.<sup>28</sup> The segregation of carbide forming elements increased the content of carbides in the central samples<sup>29</sup>

- The shower gates were used in this experiment, the molten iron had high convection intensity during the filling process. The small graphite crystals formed near mold wall drifted into the post solidified molten iron to form large-sized nodular graphite, and the nodularity and the graphite size increased.

The segregation of spheroidizing elements and carbide forming elements at the eutectic boundaries increased the chilling and the shrinkage porosity forming tendency of molten iron. Figure 9 shows the accompanying shrinkage porosity during carbide formation. The porosity can become the crack source of cast iron and reduce the properties of cast iron, especially plasticity. On the other hand, the carbide in the porosity in Figure 9 was not firmly combined with the matrix and was easy to fall off, and became an abrasive in the friction pair and accelerated the wear of cast iron.

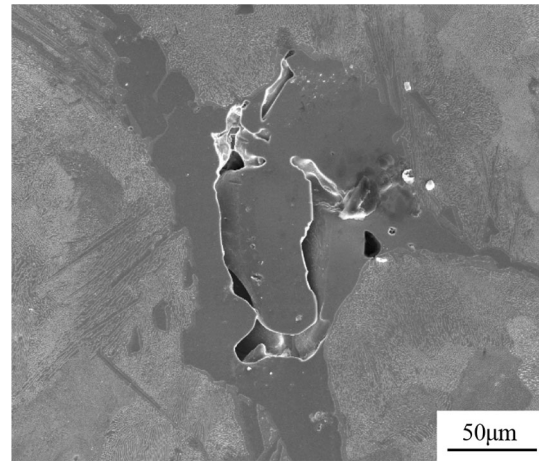


**Figure 9. Intergranular carbide and shrinkage porosity.**

## Mechanical Properties

### Mechanical Properties

Table 5 shows the tensile properties and hardness of the samples. It can be seen from Table 3 that the tensile strength, elongation, and hardness of the exterior sample were the highest among the three groups of samples. This is

**Table 5. Tensile Properties and Hardness of the Samples**

Samples	Tensile Strength/ MPa	Elongation / %	Hardness / HBW
Exterior	400 ± 5	0.52 ± 0.04	252 ± 10
Centre	383 ± 8	0.42 ± 0.02	248 ± 12
Interior	388 ± 6	0.43 ± 0.02	250 ± 10

because the exterior sample had the graphite with small size and uniform distribution, and had less carbides in matrix, while the higher hardness was related to the sound structure formed by fast cooling speed and pearlite with small spacing. The tensile properties and hardness of the interior sample were slightly lower than that of sample. However, the tensile strength, elongation, and hardness of the central sample were the lowest among the three groups of samples. The larger grain size and more carbides are the main reasons for the low properties of the central sample despite the increase in nodularity. Therefore, for heavy section CGI, it is necessary to increase the cooling rate in the center and improve the microstructure uniformity, so as to improve the uniformity of properties for the heavy section CGI.

### Fracture Morphologies

The fracture morphologies of the tensile sample are shown in Figure 10. As can be seen from Figure 10, the fracture morphologies of the three samples were cleavage facets and a small amount of torn edges, showing typical brittle fracture. It can be seen from Figure 10a that the torn edges mainly appeared at the interface between graphite and matrix. This is because a small amount of ferrite at the interface (as shown in Figure 6) was formed by plastic deformation during the tensile process. The cleavage facets appeared in the matrix which was characterized by river pattern. In Figure 10a and Figure 10c, microcracks in the fracture were clearly shown. Part of the cracks appeared at the interface between graphite and matrix, and propagated

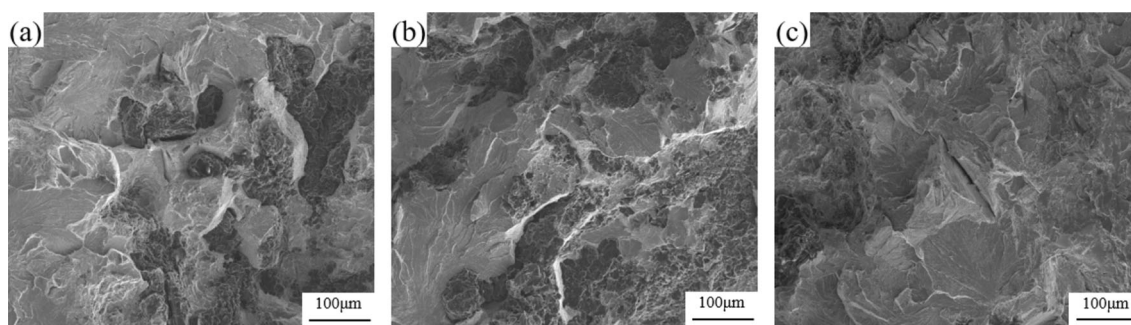
into the matrix, while another part of the cracks appeared in the matrix.

Figure 11 shows the microstructure of the longitudinal section of the sample fracture. As shown in Figure 11, the sample broke along the carbide, and the resulting crack extended interiorly along the prior austenite grain boundaries after passing through the carbide and ended at the interface between the matrix and graphite. This is because carbide is a hard brittle phase, when the stress exceeds a certain limit, it would be broken and form cracks, and the carbide crack causes the notch effect and transfers the stress to the pearlite matrix, in which the crack propagates along the prior austenite grain boundaries.

Figure 12 shows the shrinkage porosity observed in tensile fracture of the central sample. The inclusion composition in the shrinkage porosity is shown in Table 6. According to the composition in Table 4, the inclusions were mainly oxides and carbides. This was because of the slow cooling rate in center of heavy section and the high content of inclusions in the post solidified molten iron. These inclusions were enriched in the solid-liquid interface and distributed in shrinkage porosity after solidification.<sup>30,31</sup> The shrinkage porosity and inclusion are common defects in heavy section iron castings which could be alleviated by optimizing the inoculation process.<sup>32</sup> It is considered that the shrinkage porosity and inclusions are also another reason for the low mechanical properties of the central sample.

### Conclusions

In this paper, the heavy section CGI cylinder liners were prepared by using sandwich process with composite vermiculizer of REMgSiFe and RESiFe master alloys. The effect of spheroidizing element and carbide forming element segregation on the microstructure and properties of the heavy section CGI was studied, and the fracture mechanism of the heavy section CGI was discussed as well. The following conclusions were obtained.



**Figure 10. Tensile fracture morphology of the samples: (a) exterior sample, (b) central sample, (c) interior sample.**



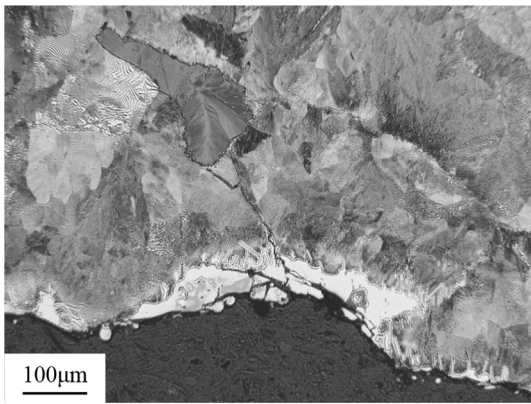


**Figure 11. Microstructure of longitudinal section of central sample fracture.**

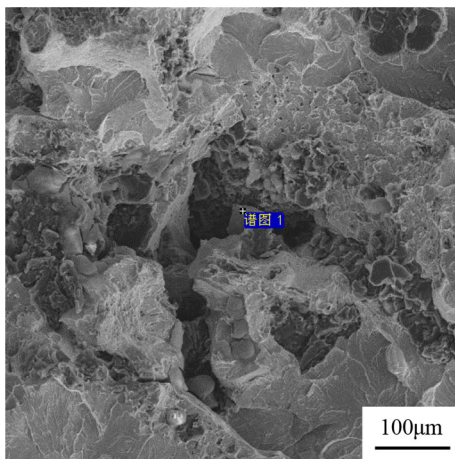


**Figure 12. The shrinkage porosity and inclusion.**

- The nodularity of heavy section of CGI cylinder liner was obviously different due to the different cooling rates and segregation of Ce and Mg. The nodularity of the exterior and interior samples was 8% and 13%, while the nodularity of the central samples was 20% and the nodule size was also larger than that of exterior and interior samples. The low cooling rate and Ce and Mg segregation promoted the formation of the bulk or nodular graphite.
- The matrix of CGI heavy section was composed of pearlite and a small amount of eutectic carbide. Carbide forming elements segregated in the final solidified molten iron increased the chilling and shrinkage porosity tendency and formed carbides at the eutectic boundary with shrinkage porosity. The carbide content of the central samples was 3%, which was higher than 2.1% of the exterior samples and 2.5% of the interior samples.
- The tensile strength, elongation, and hardness of the central samples were only 383 MPa, 0.42%, and 248 HBW, respectively, which were lower than 400 MPa, 0.52%, and 252 HBW of the

**Table 6. Inclusion Composition**

Elements	wt%	at%
C	5.75	13.22
O	26.12	45.08
Al	6.60	6.75
Ti	57.60	33.20
Mo	0.89	0.26
Fe	3.04	1.50

exterior samples and 388 MPa, 0.43%, and 250 HBW of the interior samples. The larger grain size, more carbides and shrinkage porosity reduced the tensile properties of the central samples of heavy section.

- The fracture morphologies of the samples were cleavage and a few torn edges, which showed the typical brittle fracture. The eutectic carbides and shrinkage porosities in the microstructure promoted the initiation and propagation of cracks.

### Acknowledgement

The authors were indebted to the Analytical and Testing Center of Huazhong University of Science and Technology for their help on the FESEM/FTEM characterization, and they were also grateful to State Key Laboratory of Material Processing and Die & Mould Technology in Huazhong University of Science and Technology for their support on the mechanical property tests.

**Conflict of interest** The authors declare no conflicts of interest.

### REFERENCES

1. G.Q. Shi, Z. Yang, J.P. Li et al., Investigation into the evolution of microstructure and mechanical properties of compacted graphite iron under elevated temperature. *J. Mater. Eng. Perform.* **30**, 8479–8489 (2021). <https://doi.org/10.1007/s11665-021-06068-6>
2. S. Dawson, T. Schroeder, Practical applications for compacted graphite iron. *AFS Trans.* **47**, 1–9 (2004)
3. D. Holmgren, A. Diószegi, I.L. Svensson, Effects of nodularity on thermal conductivity of cast iron. *Int. J. Cast. Met. Res.* **20**, 30–40 (2007). <https://doi.org/10.1179/136404607X202690>
4. S. Venugopal Rao, M. Venkataramana, A.C.S. Kumar, Friction and dry sliding wear properties of compact graphite iron at room temperature and 100 °C. *Mater. Today Proc.* **3250–3254**, 45 (2021). <https://doi.org/10.1016/j.matpr.2020.12.385>
5. J.L. do Vale, M. Cortz, V.M.S. Bertolini et al., Comparison of scratch resistance of lamellar and

- compacted graphite irons used in cylinder liners. *J. Braz. Soc. Mech. Sci. Eng.* **3981–3988**, 39 (2017). <https://doi.org/10.1007/s40430-016-0690-8>
6. S. Skvarenina, Y.C. Shin, Laser-assisted machining of compacted graphite iron. *Int. J. Mach. Tool Manuf.* **7–17**, 46 (2006). <https://doi.org/10.1016/j.ijmactools.2005.04.013>
  7. M.X. Zhang, J.C. Pang, L.J. Meng et al., Study on high-cycle fatigue fracture mechanism and strength prediction of RuT450. *Mater. Sci. Eng. A* **821**, 141599 (2021). <https://doi.org/10.1016/j.msea.2021.141599>
  8. N.P. Kyrtatos, Hercules A-B-C, A 10-year major R&D effort towards the next generation large marine diesel engines. *Transport Res. Arena* **48**, 1068–1077 (2012). <https://doi.org/10.1016/j.sbspro.2012.06.1083>
  9. S. Liu, L. Leng, W.J. Zhou, L. Shi, Optimizing the exhaust system of marine diesel engines to improve low-speed performances and cylinder working conditions. *Fluid Dyn. Mater. Proc.* **17**, 683–695 (2021)
  10. R. Varbanets, O. Fomin, V. Pistek et al., Acoustic method for estimation of marine low-speed engine turbocharger parameters. *J. Mar. Sci. Eng.* **9**, 321 (2021). <https://doi.org/10.3390/jmse9030321>
  11. G. Gumienny, B. Kacprzyk, J. Gawroński, Effect of copper on the crystallization process, microstructure and selected properties of CGI. *Arch. Found. Eng.* **17**, 51–56 (2017). <https://doi.org/10.1515/afe-2017-0010>
  12. G. Gumienny, B. Kurowska, P. Fabian, Compacted graphite iron with the addition of tin. *Arch. Found. Eng.* **20**, 15–20 (2020). <https://doi.org/10.24425/afe.2020.133323>
  13. V.L. Diaconu, T. Sjoren, P. Skoglund, A. Dioszegi, Influence of molybdenum alloying on thermomechanical fatigue life of compacted graphite irons. *Int. J. Cast. Met. Res.* **25**, 277–286 (2012). <https://doi.org/10.1179/1743133612Y.0000000021>
  14. Y.H. Shy, C.H. Hsu, S.C. Lee, C.Y. Hou, Effects of titanium addition and section size on microstructure and mechanical properties of compacted graphite cast iron. *Mater. Sci. Eng. A* **278**, 54–60 (2000)
  15. R. Ghasemi, L. Elmquist, H. Svensson et al., Mechanical properties of solid solution-strengthened CGI. *Int. J. Cast. Met. Res.* **29**, 97–104 (2016). <https://doi.org/10.1080/13640461.2015.1106781>
  16. M. König, M. Wessen, Influence of alloying elements on microstructure and mechanical properties of CGI. *Int. J. Cast. Met. Res.* **23**, 97–110 (2010). <https://doi.org/10.1179/136404609X12505973098972>
  17. M. Selin, D. Holmgren, I.L. Svensson, Influence of alloying additions on microstructure and thermal properties in compact graphite irons. *Int. J. Cast. Met. Res.* **22**, 283–285 (2009). <https://doi.org/10.1179/136404609X367984>
  18. S. Boonmee, D. Stefanescu, On the mechanism of casting skin formation in compacted graphite cast iron. *Int. J. Metalcast.* **3**, 19–24 (2009). <https://doi.org/10.1007/BF03355455>
  19. D. Stefanescu, S. Wills, J. Massone et al., Quantification of casting skin in ductile and compacted graphite irons and its effect on tensile properties. *Int. J. Metalcast.* **2**, 7–28 (2008). <https://doi.org/10.1007/BF03355433>
  20. W. Baer, Chunky graphite in ferritic spheroidal graphite cast iron: formation, prevention, characterization, impact on properties: an overview. *Int. J. Metalcast.* **14**, 454–488 (2020). <https://doi.org/10.1007/s40962-019-00363-8>
  21. R. Nakamura, A. Iwabuchi, M. Uchidate, Role of graphite on tribological behavior of cast iron. *Trans. JPN. Soc. Mech. Eng. C* **76**, 618–623 (2010). **(in Japanese)**
  22. D. Wollmann, G. Pintaude, Tribological performance of high-strength cast iron in lubricated contact containing carbon black. *Wear* **476**, 203743 (2021). <https://doi.org/10.1016/j.wear.2021.203743>
  23. Y. Lyu, Abrasive wear of compacted graphite cast iron with added tin. *Metallogr. Microsc. Anal.* **8**, 67–71 (2019). <https://doi.org/10.1007/s13632-018-0504-8>
  24. Q.G. Li, Y.A. Zhang, Y.N. Zhang, Influence of Sn and Nb additions on the microstructure and wear characteristics of a gray cast iron. *Appl. Phys. A* **126**, 282 (2020). <https://doi.org/10.1007/s00339-020-03468-8>
  25. M. König, M. Wessen, I.L. Svensson. Modeling of ferrite growth in compacted graphite iron, in *Proceedings of Modeling of Casting, Welding, and Advanced Solidification Processed-XII* (2009), pp. 505–512
  26. S.C. Zhao, An understanding of reverse chill and bright spots in RE-Mg nodular iron castings. *Mod. Cast. Iron* **6**, 63–65 (2005). **((In Chinese))**
  27. D.M. Stefanescu, R. Suarez, S.B. Kim, 90 years of thermal analysis as a control tool in the melting of cast iron. *China Found.* **17**(2), 69–84 (2020). <https://doi.org/10.1007/s41230-020-0039-x>
  28. L. Ceschini, A. Morri, A. Morri, E. Salsi, R. Squatrito, I. Todaro, L. Tomesani, Microstructure and mechanical properties of heavy section ductile iron castings: experimental and numerical evaluation of effects of cooling rates. *Int. J. Cast Met. Res.* **28**(6), 365–374 (2015)
  29. W.S. Chang, C.M. Lin, T.S. Lei, Effect of convection and cooling on microstructure of mid-chilled solidified casting. *Int. J. Cast. Met. Res.* **27**(2), 122–128 (2014). <https://doi.org/10.1179/1743133613Y.0000000087>
  30. E.S. Kweon, D.H. Roh, S.B. Kim, D.M. Stefanescu, Computational modeling of shrinkage porosity formation in spheroidal graphite iron: a proof of concept and experimental validation. *Int. J. Metalcast.* **15**(2), 538–547 (2021). <https://doi.org/10.1007/s40962-020-00473-8>
  31. Y. Takemoto, M. Mizumoto, K. Kinno, Interior porosity defects in ductile cast irons. *Int. J. Metalcast.*

15(3), 916–929 (2021). <https://doi.org/10.1007/s40962-020-00527-x>

32. A.K. Ramos, A. Diószegi, W.L. Guesser et al., Microstructure of compacted graphite iron near critical shrinkage areas in cylinder blocks. *Int. J. Metalcast.* **14**, 736–744 (2020). <https://doi.org/10.1007/s40962-019-00403-3>

**Publisher's Note** Springer Nature remains neutral with regard to jurisdictional claims in published maps and institutional affiliations.